2D Film of Carbon Nanofibers Elastically Astricted MnO microparticles: A Flexible Binder-Free Anode for Highly Reversible Lithium Ion Storage

Ting Wang, Hangang Li, Shaojun Shi, Ting Liu, Gang Yang, Yimin Chao*, and Fan Yin*

T. Wang, H. Li, Dr. S. Shi, T Liu, Prof. G. Yang

Jiangsu Laboratory of Advanced Functional Material, School of Chemistry and Materials Engineering, Changshu Institute of Technology, Changshu 215500, P. R. China

Email: gyang@cslg.edu.cn

Dr. Y. Chao

Energy Materials Laboratory, School of Chemistry, University of East Anglia, Norwich NR4 7TJ, UK

Email: y.chao@uea.ac.uk

Prof. F. Yin

Jiangsu Laboratory of Advanced Functional Material, School of Chemistry and Materials Engineering, Changshu Institute of Technology, Changshu 215500, P. R. China

Keywords: lithium-ion batteries; flexible films; binder-free anode materials; composite structure; electrochemical performance.

Abstract:

MnO as anode materials has received particular interest owing to its high specific capacity, abundant resources and low cost. However, it is still a serious problem that large volume change (>170%) during the lithiation/delithiation processes results in poor rate capability and fast capacity decay. With homogenous crystals of MnO grown in the network of carbon nanofibers(CNF)，binding effect of CNFs can effectively weaken the volume change of MnO during cycles. In this work, CNF/MnO flexible electrode for lithium-ion batteries is designed and synthesized. The carbon nanofibers play the roles of conductive channel and elastically astricting MnO particles during lithiation/delithiation. CNF/MnO as binder-free anode delivers specific capacity of 983.8 mAh g^{-1} after 100^{th} cycle at a current density of 0.2 A g^{-1}, and 600 mAh g^{-1} at 1 A g^{-1} which are much better than those of pure MnO and pure CNF. The ex-situ FESEM images of CNF/MnO clearly show the relative volume change of MnO/CNF as anode under various discharging and charging time. CNFs can elastically buffer the volume change of MnO during charging/discharging cycles. This work presents a facile and scalable approach for synthesizing a novel flexible binder-free anode of CNF/MnO for potential application in highly reversible lithium storage devices.

1. Introduction

Lithium-ion batteries (LIBs) possess increasing applications in electric vehicles and electricity storage stations after been widely used in portable electronic devices and electric tools.[1] Currently, commercialized graphite is the most widely used anode material for LIBs, but it cannot meet the requirements for high-energy-density batteries due to its relatively low theoretical specific capacity (372 mAh g^{-1}) and serious safety issues.[2] Therefore, the ongoing effort to find alternative anode materials with high specific capacity and good cycling stability has become intensive interest in research community worldwide.

Transition metal oxides (M_xO_y; M = Sn, Ti, Fe, Co, Ni, Mn, Mo, etc.) have been widely studied as potiential anode for LIBs.[3] Among these transition metal oxides, manganese oxides (MnO_x), have received extensive research interest due to their relatively low thermodynamic equilibrium voltage versus Li/Li^+, as well as their environmental benignity, low cost and greatnatural abundance.[4] However, MnO_x suffers from a large volumetric variation and gradual agglomeration of metal grains that result in rapid capacity decreasing and the poor rate capability during the charge/discharge processes. To address these critical challenges, earlier researchers have done excellent work on MnO_x through graphene modification, carbon coating or carbon nanofiber loading for LIBs to suppress the pulverization problem and capacity decreasing.[5]

More recently, flexible electrodes includes the anodes of MnO_x have been attractive for high-performance energy storage devices.[6] In conventional processing of electrodes, the active materials are usually attached to the current collectors using poly(vinylidene fluoride) (PVDF) as binder, solvent of N-methyl-2-pyrrolidone (NMP) and conductive additives (carbon black) for improving mechanical adhesion and electrical contact. However, the

addition of polymer binder inhibits the ion transport in the electrolyte and degrades the electrical conductivity, leading to an obvious capacity loss. Much effort has been devoted to synthesize binder-free electrodes. For examples, carbon cloth, carbon paper or nickel foam have been utilized as substrates to load metal oxides.[7] These composites are stable and flexible, but the problems such as very low weight load of metal oxides and the large thickness at millimeter level of the substrate, seriously limit the practical applications in high-performance LIBs. Carbon nanotube or graphene can also serve as substrate to load metal oxides, and the composite films can be synthesized in micrometer thickness, but the flexibility of the binder-free film is very sensitive to the weight load of metal oxide, even at very low loading.[8]

Carbon nanofibers (CNFs) are potential substrate for flexible electrodes. There are many reports in literature that metal oxide has been embedded in CNFs synthesized by electrospinning/carbonization.[4b,5d,9] The typical procedures include electrospinning and high heat-treatment, crystal growth of metal oxide and simultaneous carbonization of polyacrylonitrile (PAN) to form composite film of metal oxide embedded in CNF.[10] Although the built-in structure of the composite is still not good for high-performance LIBs, CNF film is an applicable multi-level network with micrometers free space for loading metal oxide particles. Importantly, CNFs play the roles of good conductive channel,[9b,11] and strapping the particles of metal oxide to constrain the volume change during lithiation/delithiation.

In this work, flexible CNF film has firstly been synthesized by electrospinning and carbonization, and then MnO particles are grown on CNFs and are strapped in the matrix of CNFs through hydrothermal method. The produced flexible film of metal oxide@CNF is flexible and could be used as binder-free anode without using traditional polymeric binder, conductive carbon and metal current collector, in which the energy density of electrode is

much higher than that of pure metal oxide. Owing to the unique flexible hybrid structure, the as-prepared CNF/MnO served as an anode for LIBs exhibits high reversible capacity, excellent rate and cycling performance.

2. Results and Discussion

2.1 Structure and Morphology

The crystal morphologies of pure MnO and composite of CNF/MnO are shown in **Figure 1** Pure MnO is green colored powder and cubic microcrystals (**Figure 1 a**). The average crystal size of MnO is about 10 μm. Based on the high-magnified SEM image, MnO microcrystal is close packed by nano-crystallites. Poor conductivityis predicted in the micro-sized MnO because the crystal structure is too large and full of nanopores among crystallites. If CNF film is presented in the reaction system of MnO, CNF plays a large effect in the crystal growth of MnO (as shown the SEM image in **Figure 1b and 1b'**). Homogeneous cubic nanocrystals MnO particles grow on CNF, and the crystal size of MnO is about 2 μm in CNF/MnO, much smaller than 10 μm in pure MnO sample. Millimeter sized CNF/MnO is a black colored flexible film, which can be directly applied as binder-free anode assembled in LIBs. The SEM image (Figure 1 b) of CNF/MnO film presents many free spaces within the three-dimensional (3D) matrix which providesufficient area for the growth of metal oxides. **Figure 1c** shows the XRD patterns of pure CNFs film, pure MnO powder and CNF/MnO film. Pure CNF film presents the typical widened diffraction peak (2θ) observed at 24.3° that is ascribed to the characteristic peak of graphite structure.[12] All the diffraction peaks of pure MnO powder can be readily indexed to cubic MnO (JCPDS No. 07-0230). The XRD patterns of CNF/MnO exhibit the combination of MnO and CNFs film without any impurities. A weak diffraction peak observed at 24.3° of CNF/MnO indicates that CNFs maintain graphitization structure during hydrothermal and calcination processes. The elemental mapping images of CNF/MnO

further reveal MnO particles inside the CNFs matrix. C, O and Mn elements are properly dispersed in CNFs and MnO, respectively (Figure 1c'). The carbon content by elemental analysisis calculated as 30.66 *wt*% in CNF/MnO, corresponding to weight ratio of CNF : MnO 1 : 1.5. The weight load of MnO in the flexible films of CNF/MnO is much higher than that of other composite film using carbon paper, carbon cloth or nickel foam as substrate.[7a,b,c,13]

The TEM images show that MnO crystals have closely grownaround carbon nanofibers (**Figure S1a and S1b**). Main crystal of MnO is a single crystal as shown in HR-TEM image of MnO (**Figure S1c**). The lattice spacing between fringes of MnO in the film CNF/MnO can be resolved as 0.25 nm (Figure S1c), agreeing well with inter planar spacing of (111) planes of MnO.[14] At the edge between CNF and MnO, minor MnO crystallites are dispersed on the surface of CNFs (**Figure S1d**). X-ray photoelectron spectra (XPS) of CNF/MnO show the presence of C, N, O and Mn elements without any impurities (**Figure S2**). The high-resolution spectrum of C 1s can be revolved into three peaks centered at 284.8, 286.2 and 288.3 eV, respectively. The main peak at 284.8 eV belongs to the sp^2-hybridized graphite carbon.[15] Two weak peaks at 286.2 and 288.3 eV belong to C-O and C=O, respectively. [16] The N 1s core-level spectrum can be well fitted into a pyrodinic nitrogen (N-6) at 398.4 eV and a pyrrolic nitrogen (N-5) at 400.4 ev.[17] The presence of C, N elements observed in CNF/MnO are in accordance with CNFs produced by PAN. The binding energy of O1s obtained here are 529.9 eV and 531.5eV that can be assigned to Mn-O and C-O bonding, respectively. The oxidation state of Mn determined by analyzing the spin energy separation of Mn 3s doublet spectrum, exhibits a typical spin energy separation of 5.9 eV corresponding to Mn(II).[18] The high-resolution spectra of Mn2p exhibit two peaks at 641.5 eV for Mn $2p_{3/2}$ and 653.2 eV for Mn $2p_{1/2}$, respectively, which are also consistent with those of MnO.

2.2 Electrochemical Performance

The flexible film of CNF/MnO is directly assembled in LIBs without using any polymeric binders, conductive additives or current collector. The CV profiles of CNF/MnO are shown in **Figure 2a**. A weak reduction peak at 0.5 V is ascribed to the formation of solid electrolyte interface (SEI) layers.[19] The sharp reduction peak closed to 0.1 V in the first sweep is ascribed to the reduction of Mn^{2+} to Mn^0. This peak shifts to 0.3 V in the following cycles, suggesting an irreversible phase transformation due to the formation of Li_2O and metallic manganese.[20]A wide peak around 1.3 V appearing in anodic sweep is ascribed to the oxidation of Mn(0) to Mn(II).[21] The profiles of CVs in the subsequent sweep are overlapped very well except the initial sweep, demonstrating the excellent reversibility of the electrochemical reactions happened in the electrode CNF/MnO. GITT technique based on chronopotentiometry has been carried out to study the diffusion ability of lithium ions during charge/discharge processes.[22] According to the GITT curves (**Figure 2b**), the D_{Li}^+ values of pure MnO and CNF/MnO are calculated and plotted in **Figure 2c**, **2d**. In the discharge process, the D_{Li}^+ rapidly decreases to the minimum at 0.7 V and then rapidly increases back. Pure MnO presents much lower D_{Li}^+ than CNF/MnO, especially the D_{Li}^+ of MnO is lower than that of CNF/MnO three orders of magnitude at 0.7 V (Figure 2c). In charge process, pure MnO also appears lower D_{Li}^+ than CNF/MnO (Figure 2d). It further confirms that CNFs not only provides conductive channel but also enhances the contact between MnO particles and electrolyte improving the diffusion ability of Li^+ during lithiation/delithiation processes.

The charge-discharge profiles of CNF/MnO, pure MnO and pure CNF at a current density of 0.2 A g^{-1} between 0.001 and 3.0 V are displayed in **Figure 3a**. The initial discharge capacities of pure MnO, pure CNF and CNF/MnO are 933.1, 595.3 and 1308.3 mAh g^{-1}, respectively. The specific capacity of CNF/MnO is calculated by using the following equation.[23]

$$C_{CNF/MnO} = C_{MnO} \times \%\text{mass of MnO} + C_{CNFs} \times \%\text{mass of CNFs}$$

As shown in Figure 3a, the initial Coulombic efficiencies of pure MnO, pure CNF and CNF/MnO are 50%, 62% and 67%, respectively. Capacity losses in the first cycle appeared in the three samples are mainly attributed to the irreversible processes such as electrolyte decomposition and inevitable formation of the solid electrolyte interphase (SEI) layer,[24] but the columbic efficiency of CNF/MnO is close to 100% after the initial cycles. After the first lithiation, the SEI layer covers the surface of MnO particles which hinders the direct contact between the resulting nanoclusters of Mn and the electrolyte.[25] Moreover, CNF/MnO shows excellent cycling stability (**Figure 3b**). At the 50th cycle, CNF/MnO remains a capacity of 992.3 mAh g^{-1}, but the capacity decreases to 332.1 mAh g^{-1} for pure MnO and 280 mAh g^{-1}forpure CNF, respectively. Under various current densities, CNF/MnO presents best rate performance than those of pure MnO and pure CNF, respectively (**Figure 3c**). The capacities for CNF/MnO at 0.05, 0.2 and 1 A g^{-1} are 1004.4, 948.4, and 646.0mAh g^{-1}, respectively. However, both pure MnO and pure CNF electrodes only deliver 195 mAh g^{-1} at the current density of 1 A g^{-1}. A capacity of 1318 mAh g^{-1} can be restored after another 25 cycles when the rate performed with CNF/MnO electrode goes back to 0.05 A g^{-1}. The excellent specific capacity, cyclic stability and rate performance, can be attributed to the synergetic structure of CNF/MnO in which CNFs provide excellent conductive channel improving the specific capacity and effective matrix buffering the volume change to promote the cyclic performance. The comparison in electrochemical properties between CNF/MnO and other related works has been summarized in Table S1 (in Supporting Information).

Electrochemical impedance spectroscopy (EIS) of MnO and CNF/MnO carried out at the states of the 4th and 20th discharge is shown in **Figure 4** with fittings on the basis of an equivalent circuit model (**the inset in Figure 4b**). The intercept of the high-frequency semicircle on the Z' axis is attributed to the resistance of electrolyte (R_s). The high-frequency semicircle corresponds to the SEI layer resistance (R_{SEI}). The middle-frequency semicircle is

associated with the charge transfer resistance (R_{ct}) and the electric resistance (R_e). The 45° slope line is generally defined as Warburg impedance (Z_w) at low frequency, denoting the resistance caused by ion diffusion.[26] The fitted EIS parameters are listed in Table 1. The resistances of CNF/MnO are lower than those of pure MnO. For example, R_{ct} of CNF/MnO is 27.42 ohms much lower than 96.98 ohms of MnO at the state of discharged fourth cycles. CNF matrix plays the important role of improving the conductivity of MnO particles. For more cycles, the resistances of R_{sei}, R_e, R_{ct} and W-r of MnO are all increased from 8.596, 35.68, 96.98 and 183.6 ohms at the 4th cycle, to 84.1, 138.5, 3660 and 200.6 ohms at the 20th cycle. However, the resistances of R_{sei}, R_e, R_{ct} and W-r of CNF/MnO present minor change after dozens of cycles, 8.704, 27.16, 27.42 and 96.1 ohms at the 4th cycle, and 12.73, 9.614, 40.9 and 103.6 ohms at the 20th cycle, respectively. The structure of CNFs bound MnO particles **(the inset of Figure 4a**) efficiently locks and stabilizes MnO during charge/discharge processes. The flexible spaces within the CNFs matrix buffer the volume change of MnO during lithiation/delithiation cycles.

2.3 Charge-Discharge Process of Hybrid Composites

FESEM images of CNF/MnO electrodes at various lithiation/delithiation states clearly demonstrate the effect of CNFs strapping MnO particles. In **Figure 5**, *ex-situ* FESEM images are shown from four CNF/MnO electrodes discharged for 1 h, 3 h, 9 h, and 14 h, respectively. It is clearly observed that MnO crystals remain completely particles morphology during discharge process. With the increased discharge time, MnO crystals display sizes at 2.39, 3.32, 3.57, and 5.01 μm after discharged for 1 h, 3 h, 9 h, and 14 h, respectively. Carbon nanofibers like elastic ropes to strap the enlarged MnO particles, avoiding the pulverization of MnO particles. The elemental mappings of CNF/MnO film reveal a homogeneous distribution of C, O and Mn elements, indicating a stability of both hybrid structure and composition of

CNF/MnO electrode. Minor F element appeared on the surface of MnO particles due to the formation of SEI film.

To find the reversible volume change of CNF/MnOanode during charging processes, FESEM images shown in **Figure 6** are from another set of four CNF/MnO anodes charged for 6 h, 8 h, 9 h, and 13 h, respectively. With the increased charging time, MnO crystals dispersed in CNF matrix present the gradually decreased particle size, 4.95, 3.47, 2.65 and 2.44 μm, respectively. Flexible carbon nanofibers still strap MnO particles. The elemental mappings of CNF/MnO film reveal a homogeneous distribution of C, O and Mn elements. The CNFs matrix provides enough elasticity space for volume change of MnO during discharge/discharge processes. It should be concluded that carbon nanofibers in such well-designed CNF/MnO hybrid film efficiently buffer the stress of MnO particle during lithiation/delithiation processes.

As a comparison, pure MnO electrode dispersed in the binder of PVdF and conductive carbon after cycles presents pulverization and irregular crystals (**Figure S3**). This is a strong proof supporting the capacity fading of pure MnO during dozens of cycles. **Figure 7** exhibits the *ex-situ* FESEM images of CNF/MnO electrode discharged to 0.001 V at the 50thcycle. Even the crystal size of MnO reaches to 5.1 μm, the MnO crystals are still ordered cubic particles and separately strapped by carbon nanofibers. There are two advantages in stability appeared in the hybrid structure of CNF/MnO. Firstly, CNF matrix provides enough elastic space for volume change of MnO during discharge/discharge processes; the second, MnO strapped by CNFs efficiently stops the pulverization of particles and lost from the matrix. **Figure 7c** is a good example to show one MnO particle strapped by several elastic carbon nanofibers. The corresponding elemental mapping reveals a homogeneous dispersion of C, O, Mn elements and the stable hybrid structure (**Figure 7d**). TEM images clearly reveal the morphologies of

MnO crystal and CNF/MnO film as anode discharge for 50 cycles. The body of MnO is still solid crystal except a loose thin layer on the surface (**Figure 7e**). Furthermore, carbon nanofiber presents a little increase in diameter because CNFs also involve in the lithiation/delithiationin addition to the role as conductive matrix loading MnO crystals (**Figure 7f**).

XPS on CNF/MnO film at the state of 50^{th} discharge is displayed in **Figure 8**. **Figure 8a** shows the XPS survey spectrum after different Ar^+ ion sputtering times. With the extending of etching time, the Mn2p peaks have been gradually strengthened to a stable state as the SEI film completely removed. Before and after Ar^+ etching, the main component on the surface of CNF/MnO electrode is Li_2CO_3 presented a large Li1s peak at the binding energy of 55.0 eV (**Figure 8b**). [27] After Ar^+ etching for 270 seconds, a weak peak appears at the binding energy of 53.16 eV attributed to the existence of Li_2O. The C1s and O 1s XPS from fresh CNF/MnO film present the characteristic strong peaks (**Figure 8c, 8d**), for example C sp^2 from CNFs observed at 284.8 eV. After 50 cycles lithiation, C sp^2 from CNF is seriously weakened but a strong C1s peak is observed at 289.9 eV attributed to the component of Li_2CO_3, owing to SEI film grown on CNF. This is the strong evidence that CNF involves in the lithiation/delithiation in addition to the role as substrate loading MnO and as conductive channel improving electrochemical properties.

3. Conclusion

In summary, the present work has demonstrated a low-cost and potentially scalable technique of synthesizing flexible CNF/MnO film as bind-free anode for LIB. In the hybrid structure of CNF/MnO, MnO particles are effectively strapped by carbon nanofibers during charge/discharge cycles. The *ex-situ* SEM images of CNF/MnO after 50 cycles clearly show

the relative volume change of MnO/CNF as anode under various discharging and charging time. The carbon nanofibers play the roles of conductive channel and confining MnO particles in CNFs matrix to buffer the volume change of MnO during lithiation/delithiation. The synthesized CNF/MnO films show a specific capacity of 823.8 mAh g^{-1} after 100th cycle at a current density of 0.2 A g^{-1}, and 600 mAh g^{-1} at 1 A g^{-1}, much better than those of pure MnO and pure CNF. The CNF matrix provides enough elasticity space for volume change of MnO during discharge/discharge processes. The crystal size of MnO, increasing during lithiation and decreasing during delithiation, has been efficiently buffered by flexible carbon nanofibers. Our one-pot synthesis route to load metal oxide in CNF is simple and industrially scalable. This work has successfully demonstrated the potential to synthesize flexible electrode with high weight loading of metal oxide for energy storage devices.

4. Experimental Section

Materials Preparation: The preparing process of CNF films includes electrospinning method and carbonization of PAN. The weight of CNFs film is 2.5 mg cm^{-2} and the size of CNFs electrodes is 1 cm in diameter. A solution included $MnCl_2$ and urea with weight ratio of 1.2 : 1 was added in a autoclave (the filling degree 70%), and CNFs films were placed in the autoclave. The hydrothermal reaction was under 200 ºC for 6 h. The resulted CNF/$MnCO_3$ film was washed for several times with distilled water and ethanol, dried in vacuum at 90 °C for 12 h. The flexible film of CNF/$MnCO_3$ was heated in N_2 atmosphere at 700 °C for 3 h, which converted to flexible CNF/MnO film. The structure and morphologies of the as-produced CNF/MnO are repeatable for three batches. As a comparison, the sample of pure MnO powder was also produced according to the previous procedure without CNF film.

Structure and Morphology Characterization: The as-synthesized products were examined by

XRD on Rigaku diffractometer (Dmax-2200) with Cu Kα radiation at 30 kV and 30 mA. The diffraction data was collected at each 0.02° step from 10° to 80°. The morphologies of the products were characterized by scanning electron microscopy (FE-SEM and EDX, SIGMA, ZEISS 20 kV), transmission electron microscopy (TEM, JEOL-2000CX, 200 kV) and high-resolution transmission electron microscopy (HRTEM, JEOL JEM-2010F, 200 kV). The elemental analysis was carried out using X-ray photoelectron spectroscopy (XPS, Thermo Scientific, Escalab250Xi, Al-Kα as radiation source). The binding energies obtained in XPS analysis were calibrated against the C1s peak that was locked at 284.6 eV. Core level peaks were deconvoluted using Gaussian−Lorentzian line shapes and Shirley background. The amounts of C, H and N elements were measured with a VarioEL III elemental analyzer (Elementar, Germany). To study the morphologies and elemental state of the electrode after lithiation/delithiation, batteries were disassembled in an Ar-filled glove box. The removed electrodes were rinsed for several times with dimethyl carbonates, and then dried in Ar-filled glove box overnight.

Electrochemical measurement: The binder-free flexible film CNF/MnO and pure carbon nanofibers film as electrode were directly assembled in a CR2016 coin cell. The coin cells (CR2016) were assembled in an Ar-filled glove box using lithium metal as the counter electrode, Celgard 2500 as the separator, and 1 M $LiPF_6$ (dissolved in ethylene carbonate, dimethyl carbonate and ethyl-methyl carbonate in a 1 : 1 : 1 volume ratio) as the electrolyte. Meanwhile, the comparison electrode of pure MnO was a mixture of 70 wt% as-synthesized sample, 20 wt% acetylene black, and 10 wt% polyvinylidenedifluoride (PVDF) in the presence of N–methyl pyrrolidinone (NMP). After being stirred overnight, the slurry was pasted onto a Cu foil, and then the electrode was dried at 120 °C under vacuum. The working area of the electrode was set at Φ1.1 cm and the weight of 3-4 mg cm^{-2}. The galvanostatic charge and discharge cycling was studied at room temperature in the voltage range 0.001−3.0

V (vs. Li^+/Li) at different current densities by LAND CT2001A battery testing system (Wuhan, China). Cyclic voltammetry (CV) was conducted on the CHI660E electrochemical workstation (Shanghai, China) between voltages 0.001 and 3.0 V (vs. Li^+/Li) at a scan rate of 0.1 mV s^{-1}. Electrochemical impedance spectroscopy (EIS) measurements were conducted using a PARSTAT2273 electrochemical workstation (Princeton Applied Research, USA), where the amplitude of the input AC signal was kept at 5 mV and the frequency range was set between 10^{-2} and 10^5 Hz. The state of the cell was full discharged before EIS measurement. Galvanostatic intermittent titration technique (GITT) was conducted at room temperature in the voltage range 0.001−3.0 V (vs. Li^+/Li).

Supporting Information

Supporting Information is available from the Wiley Online Library or from the author.

Acknowledgments

The authors acknowledge the support from the National Natural Science Foundation of China (Grant No. 51172032), Natural Science Foundation of Jiangsu Province of China (Grant No. BK20141229, BK20160404).

Received: ((will be filled in by the editorial staff))

Revised: ((will be filled in by the editorial staff))

Published online: ((will be filled in by the editorial staff))

References

[1] a) D. Larcher, J. M. Tarascon, *Nat. Chem.* **2015**, *7*, 19; b) R. Noorden, *Nature*. **2014**, *507*, 26; c) J. B. Goodenough, K. S. Park, *J. Am. Chem. Soc.* **2013**, *135*, 1167.

[2] Z. B. Yang, J. Ren, Z. T. Zhang, X. L. Chen, G. Z. Guan, L. B. Qiu, Y. Zhang, H. S.

Peng, *Chem. Rev.* **2015**, *115*, 5159.

[3] a) C. Z. Yuan, H. B. Wu, Y. Xie, X. W. Lou, *Angew. Chem. Int. Ed.* **2013**, *52*, 2; b) P. Poizot, S. Laruelle, S. Grugeon, L. Dupont, J. M. Tarascon, *Nature***. 2000**, *407*, 496; c) M. V. Reddy, G. V. SubbaRao, B. V. R. Chowdari, *Chem. Rev.* **2013**, *113*, 5364; c) Y. M. Sun, X. L. Hu, W. Luo, Y. H. Huang, *J. Mater. Chem.* **2012**, *22*, 19190; d) X. Gu, L. Chen, Z. C. Ju, H. Y. Xu, J. Yang, Y. T. Qian, *Adv. Funct. Mater.* **2013**, *23*, 4049; e) X. Gu, J. Yue, L. J. Li, H. T. Xue, J. Yang, X. B. Zhao. *Electrochim. Acta* **2015**, *184*, 250.

[4] a) J. C. Guo, Q. Liu, C. S. Wang, M. R. Zachariah, *Adv. Funct. Mater.* **2012**, *22*, 803; b) G. Yang, Y. H. Li, H. M. Ji, H. Y. Wang, P. Gao, L. Wang, H. D. Liu, J. Pinto, X. F. Jiang, *J. Power Sources.* **2012**, *216*, 353; c) Q. Sun, Z.J. Sun, Z. J. Zhang, Q. Yu, Q. Yan, J. Y. Zhang, Y. Yu, B. Xiang, *ACS Appl. Mater. Interfaces.* **2016**, *10*, 6303. d) Y. M. Sun, X. L. Hu, W.Luo, F. F. Xia, Y. H. Huang. *Adv. Funct. Mater.* **2013**, *23*, 2436; e) W. Luo, X. L. Hu, Y. M. Sun, Y. H. Huang. *ACS Appl. Mater. Interfaces* **2013**, *5*, 1997.

[5] a) Y. Xia, Z. Xiao, X. Dou, H. Huang, X. H. Lu, R. J. Yan, Y. P. Gan, W. J. Zhu, J. P. Tu, W. K. Zhang, X. Y. Tao, *ACS Nano.* **2013**, *7*, 7083; b) L. Wang, Y. H. Li, Z. D. Han, L. Chen, B. Qian, X. F. Jiang, J. Pinto, G. Yang, *J. Mater. Chem. A.* **2013**, *29*, 8385; c) S. B. Wang, Y. L. Xing, C. L. Xiao, H. Z. Xu, S. C. Zhang, *J. Power Sources.* **2016**, *307*, 11; d) L. Ji，X. Zhang; *Electrochem. Commun.* **2009**, *11*, 795. e) T. Z. Yuan, Y. Z. Jiang, W. P. Sun, B. Xiang, Y. Li, M. Yan, B. Xu, S. X. Dou; *Adv. Funct. Mater*. **2016**, *26*, 2198; f) S. B. Wang, Y. L. Xing, C. L. Xiao, H. Z. Xu, S. C. Zhang; J. Power Sources **2016**, *307*, 11.

[6] a) J. W. Qin, Q. Zhang, Z. Y. Cao, X. Li, C. W. Hua, B. Q. Wei, *Nano. Energy*.**2013**, *2*, 733; b) L. F. Chen, Z. H. Huang, H. W. Liang, Q. F. Guan, S. H. Yu, *Adv. Mater.* **2013**, *25*, 4746.

[7] a) C. Wang, W. Wan, Y. H. Huang, J. T. Chen, H. H. Zhou, X. X. Zhang, *Nanoscale*. **2014**, *6*, 5351; b) C. Z. Yuan, L. Yang, L. R. Hou, L. F. Shen, X.G. Zhang, X. W. Lou, *Energy*

Environ. Sci. **2012**, *5*, 7883; c) L. Yu, G. Q. Zhang, C. Z. Yuan, X.W. Lou, *Chem. Commun*. **2013**, *49*, 137.

[8] a) R. J. Chen, T. Zhao, W.P. Wu, F. Wu, J.Q. Li, R. Xu, H.M. Wu, H. M. Albishri, A. S. Al-Bogami, D. A. El-Hady, J. Lu, K. Amine, *Nano Lett.* **2014**, *14*, 5899; b) Y. R. Zhong, M. Yang, X. L. Zhou, Y. T. Luo, J.P. Wei, Z. Zhou, *Adv. Mater.* **2015**, *27*, 806; c) Z. P. Luo, Q. Z. Xiao, G. T. Lei, Z. H. Li, C. J. Tang, *Carbon.* **2016**, *98*, 373.

[9] a) W. Li, M. Li, M. Wang, L. Zeng, Y. Yu, *Nano Energy.* **2015,** *13*, 693; b) B. Zhang, F. Y. Kang, J. M. Tarascon, J. K. Kim, *Prog. Mater. Sci*. **2016**, *76*, 319.

[10] a) H. Y. Wang, H. Q. Huang, L. Chen, C. G. Wang, B. Yan, Y. T. Yu, Y. Yang, *ACS. Sustainable Chem. Eng.* **2014**, *2*, 2310; b) B. Liu, X. L. Hu, H. H. Xu, W. Luo, Y. M. Sun, Y. H. Huang. *Sci. Rep.* **2014**, *4*, 4229; c) J. G. Wang, Y. Yang, Z, H. Huang, F. Y. Kang, Electrochim. Acta **2015**, *170*, 164.

[11] W. Li, M. Li, M. Wang, L. Zeng, Y. Yu, *Nano Energy.* **2015**, *13*, 693.

[12] Y. Mao, H. Duan, B. Xu, L. Zhang, Y. S. Hu, C. C. Zhao, Z. X. Wang, L. Q. Chen, Y. S. Yang, *Energy Environ. Sci*. **2012**, *5*, 7950.

[13] a) C. Wang, W. Wan, Y. H. Huang, J. T. Chen, H. H. Zhou, X. X. Zhang, *Nanoscale*. **2014**, *6*, 5351; b) C. Z. Yuan, L. Yang, L.R. Hou, L.F. Shen, X.G. Zhang, X. W. Lou, *Energy Environ. Sci*. **2012**, *5*, 7883; c) L. Yu, G. Q. Zhang, C. Z. Yuan, X. W. Lou, *Chem. Commun*.**2013**, *49*, 137; d) C. X. Yang, Q. M. Gao, W. Q. Tian, Y. L. Tan, T. Zhang, K. Yan, L. H. Zhua, *J. Mater. Chem. A 2*, **2014**, 19975.

[14] X. X. Gu, J. Yue, L. Chen, S. Liu, H. Y. Xu, J. Yang, Y. T. Qian, X. B. Zhao,*J. Mater. Chem. A.* **2015**, *3*, 1037.

[15] Y. Xiao, M. Cao, *ACS Appl. Mater. Interfaces.* **2015**, *7*, 12840.

[16] D. Liu, H. Lu, H. Yang, X. L. Wu, B. H. Hou, F. Wan, S. D. Bao, Q. Y. Yan, H. M. Xie, R. S. Wang, *J. Mater. Chem. A* **2015**, 3, 19738.

[17] a) M. M. Yang, Y. R. Zhong, X. L. Zhou, J. J. Ren, L.W. Su, J. P. Wei, Z. Zhou, *J. Mater.*

Chem. A. 2, **2014**, 12519; b) D. Hulicova-Jurcakov, M. Seredych, G. Q. Lu, T. J. Bandosz, *Adv. Funct. Mater.* **2009**, *19*, 438.

[18] Y. Xiao, X. Wang, W. Wang, D. Zhao, M. Cao, *ACS Appl. Mater. Interfaces.* **2014**, *6*, 2051.

[19] J. Collins, G. Gourdin, M. Foster, D. Y. Qu, *Carbon* **2015**, *92*, 193.

[20] X. W. Li, D. Li, L. Qiao, X. H. Wang, X.L. Sun, P. Wang, D.Y. He, *J. Mater. Chem.* **2012**, *22*, 9189.

[21] B. Sun, Z. Chen, H.-S. Kim, H. Ahn, G. Wang, *J. Power Sources.* **2011**, *196*, 3346.

[22] W. Weppner, R. A. Huggins, *J. Electrochem. Soc.* **1997**, *124*, 1569.

[23] Y. Liu, N. Zhang, L. Jiao, J. Chen, *Adv. Mater*. **2015**, *27*, 6702.

[24] J. Maier, *Nat. Mater*, **2005**, *4*, 805.

[25] a) K.F. Zhong, X. Xia, B. Zhang, H. Li, Z.X. Wang, L.Q. Chen, *J. Power Sources* **2010**, *195*, 3300; b) K.F. Zhong, B. Zhang, S.H. Luo, W. Wen, H. Li, X.J. Huang, L.Q. Chen, *J. Power Sources* 2011, 196, 6802; c) X.W. Li, D. Li, L. Qiao, X.H. Wang, X.L. Sun, P. Wang, D.Y. He, *J. Mater. Chem.* **2012**, *22*, 9189. c) J. Zhang, R. Wang, X. C. Yang, W. Lu, X. D. Wu, X. P. Wang, H. Li, L. W. Chen, *Nano Lett.* **2012**, *12*, 2153.

[26] M. R. Busche, T. D. M. Schneider, M. L. Rechi, H. Sommer, D. A.Weber, M. Falk J. Janek, *Nat. Chem.* **2016**, *8*, 426.

[27] K. Edströma, M. Herstedta, D. P. Abraham, *J. Power Sources*. **2006**, *153*, 380.

Table 1 Impedance parameters fitted using equivalent circuit for CNF/MnO and pure MnO electrodes at the state of the 4th and 20th discharge.

Samples	R_s/Ω	R_{sei}/Ω	R_e/Ω	R_{ct}/Ω	W-r/Ω	$x^2/10^{-4}$
CNF/MnO 4th	6.384	8.704	27.16	27.42	96.1	1.6
MnO 4th	2.989	8.596	35.68	96.98	183.6	2.9
CNF/MnO 20th	3.418	12.73	9.614	40.9	103.6	1.2
MnO 20th	2.094	84.1	138.5	3660	200.6	1.9

Figure captions

Figure 1 SEM images of MnO (a, a') and CNF/MnO (b, b'). The insets are the digital photos of both samples, XRD patterns of MnO, pure CNF and the composite CNF/MnO (c), and the EDS mapping images of CNF/MnO (c').

Figure 2 Cyclic voltammetry profiles of flexible film CNF/MnO between 0 and 3 V at a scan rate of 0.1 mV s^{-1} (a). GITT curves (b), and diffusion coefficients of Li^+ in pure MnO, CNF/MnO at discharge (b) and charge (c) processes, respectively.

Figure 3 The initial charge/discharge profiles (a), cycling life and the corresponding Columbic efficiencies (b) of MnO, CNF/MnO and CNF carried out under the current density of 0.2 A g^{-1}.

Figure 4 EIS fitted profiles of MnO and CNF/MnO electrodes at the 4^{th} discharge state (a) and the 20^{th} discharge state (b). The inset in (a) is the schematic conductive channel for electrons and lithium ions, and the inset in (b) is the equivalent circuit fitting EIS data. Hollow dots represent the experimental data and the line represents the fitted data.

Figure 5 Low magnified (the 1^{st} line) and high magnified (the 2^{nd} line) SEM images,nd elemental mapping (the 3^{rd} line) of the flexible electrode CNF/MnO at the state of discharging 1 h (a), 3 h (b), 9 h (c), and 12 h (d), respectively.

Figure 6 Low magnified (the 1^{st} line) and high magnified (the 2^{nd} line) SEM images, and elemental mapping (the 3^{rd} line) of the flexible electrode CNF/MnO at the state of charging 6 h (a), 8 h (b), 9 h (c), and 11 h (d), respectively.

Figure 7 Low magnified (a) and high magnified (b) SEM images, elemental mapping (c, d), and TEM images (e, f) of the flexible electrode CNF/MnO at the state of 50^{th} discharge.

Figure 8 XPS wide scan survey of an electrode CNF/MnO at the state of 50^{th} discharging after Ar^+ etching for 0 - 270 s (a). XPS spectrum Li 1s (b), C 1s (c), and O 1s (d) without Ar^+ etching and with 270 s Ar^+ etching.

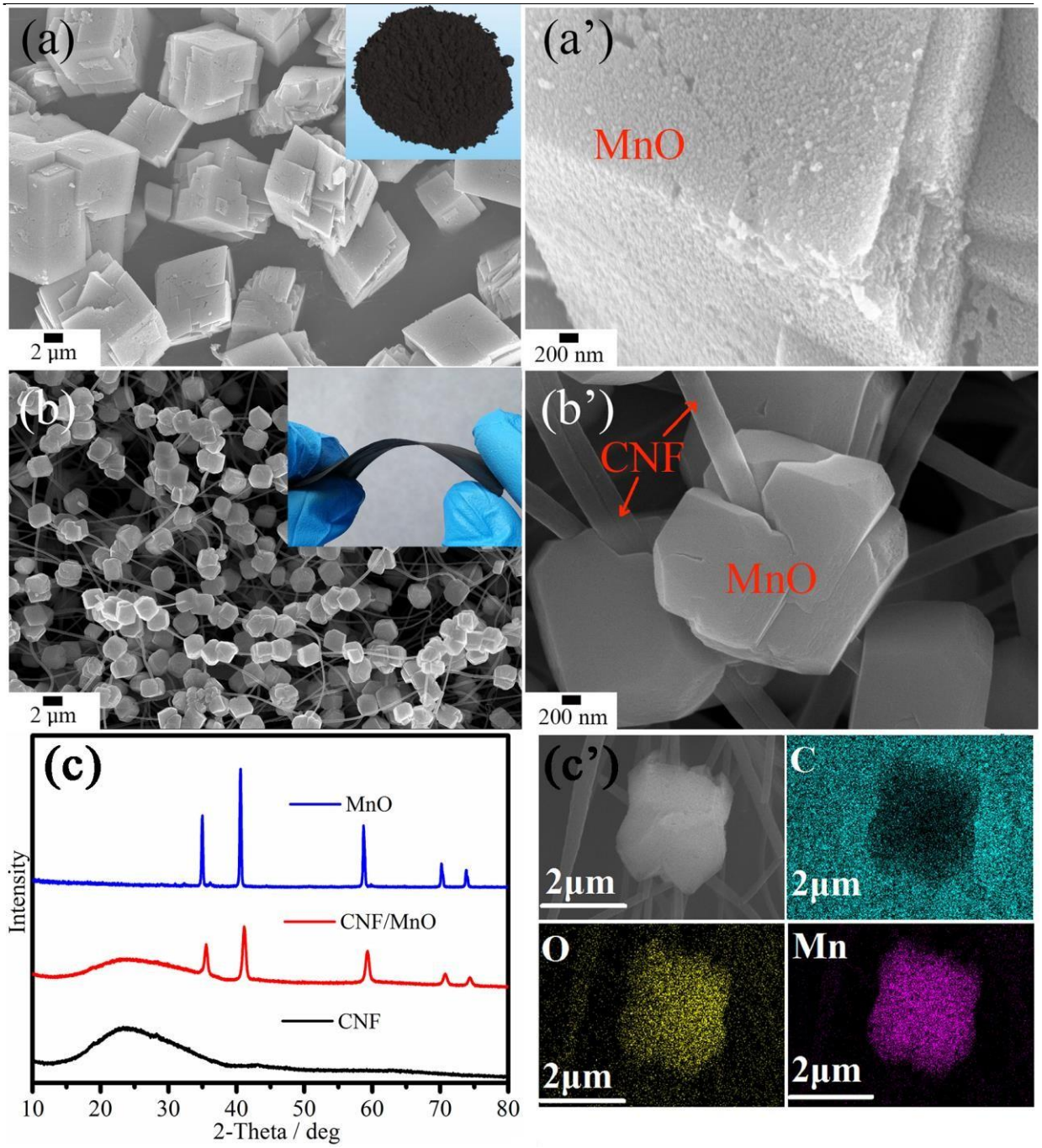

Figure 1 SEM images of MnO (a, a') and CNF/MnO (b, b'). The insets are the digital photos of both samples, XRD patterns of MnO, pure CNF and the composite CNF/MnO (c), and the EDS mapping images of CNF/MnO (c').

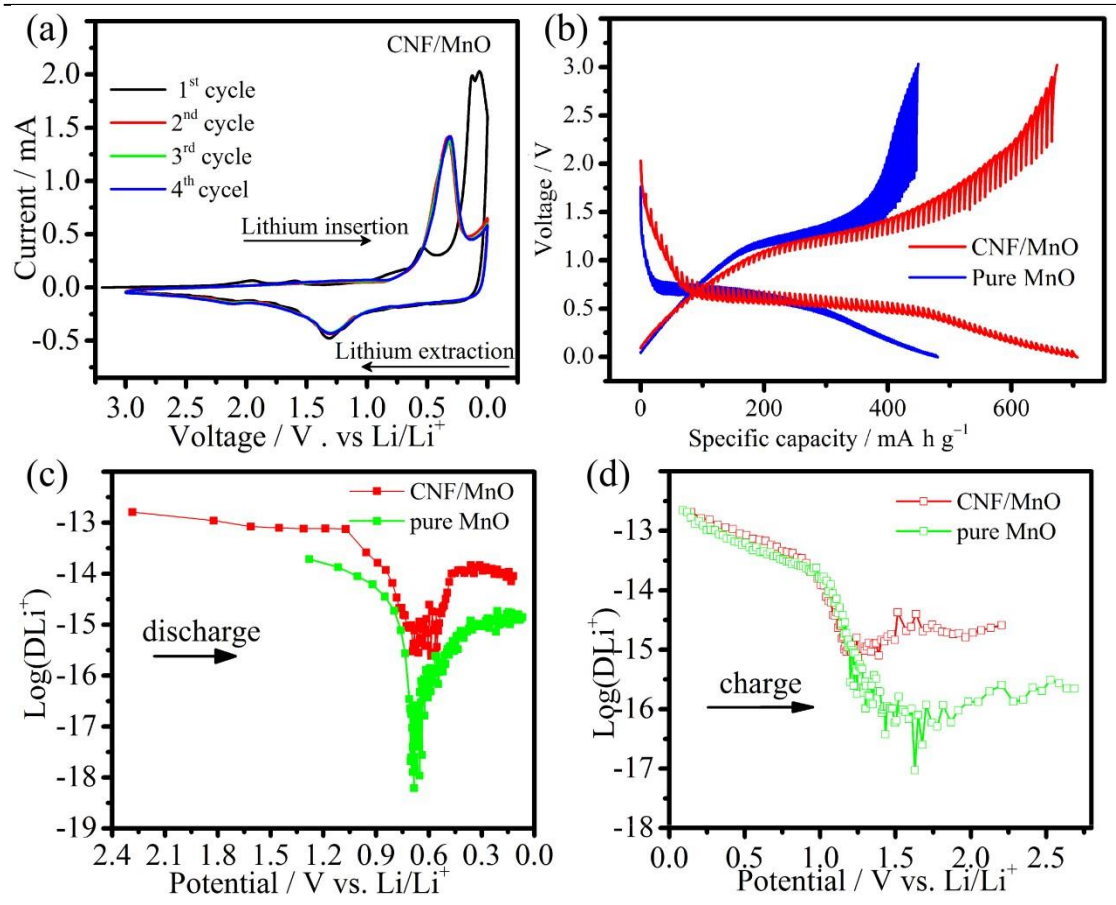

Figure 2 Cyclic voltammetry profiles of flexible film CNF/MnO between 0 and 3 V at a scan rate of 0.1 mV s^{-1} (a). GITT curves (b), and diffusion coefficients of Li^+ in pure MnO, CNF/MnO at discharge (c) and charge (d) processes, respectively.

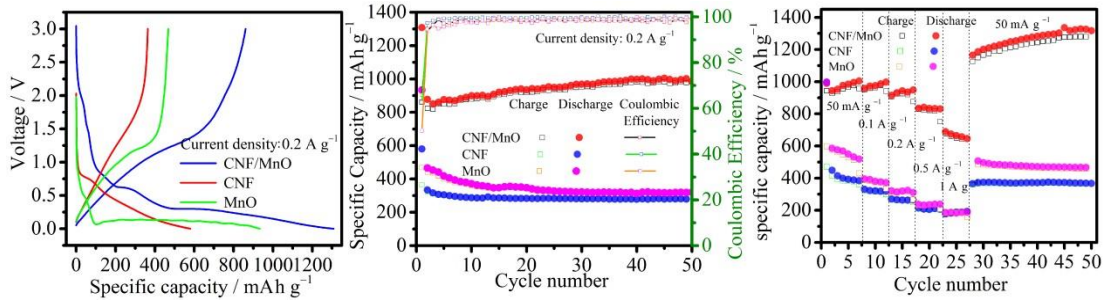

Figure 3 The initial charge/discharge profiles (a), cycling life and the corresponding Columbic efficiencies (b) of MnO, CNF/MnO and CNF carried out under the current density of 0.2 A g^{-1}.

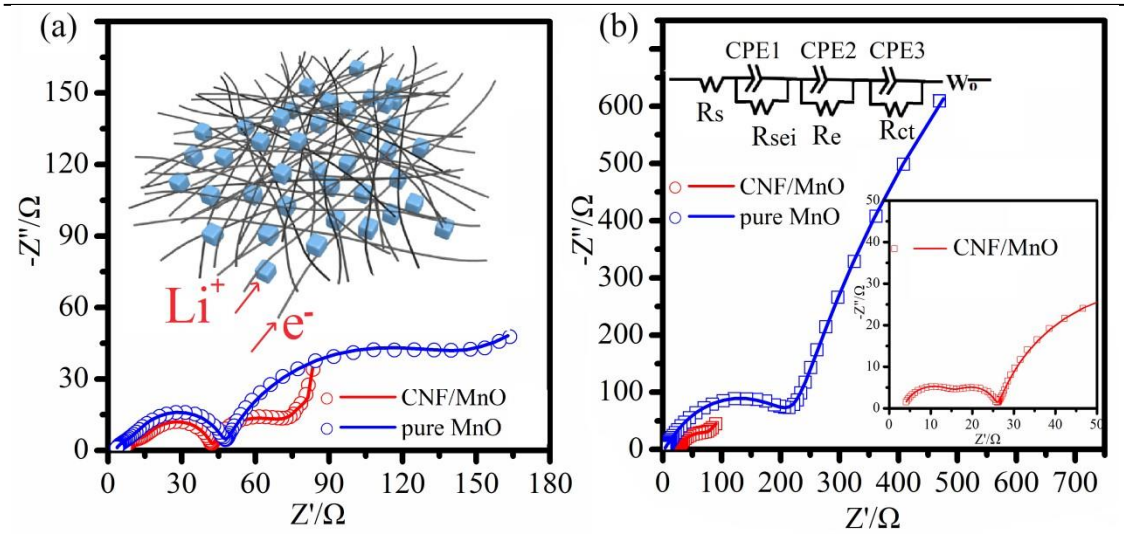

Figure 4 EIS fitted profiles of MnO and CNF/MnO electrodes at the 4th discharge state (a) and the 20th discharge state (b). The inset in Figure 4a is the schematic conductive channel for electrons and lithium ions, and the insets in Figure 4bare the equivalent circuit and the enlarged Nyquist plot of CNF/MnO. Hollow dots represent the experimental data and the lines represent the fittings.

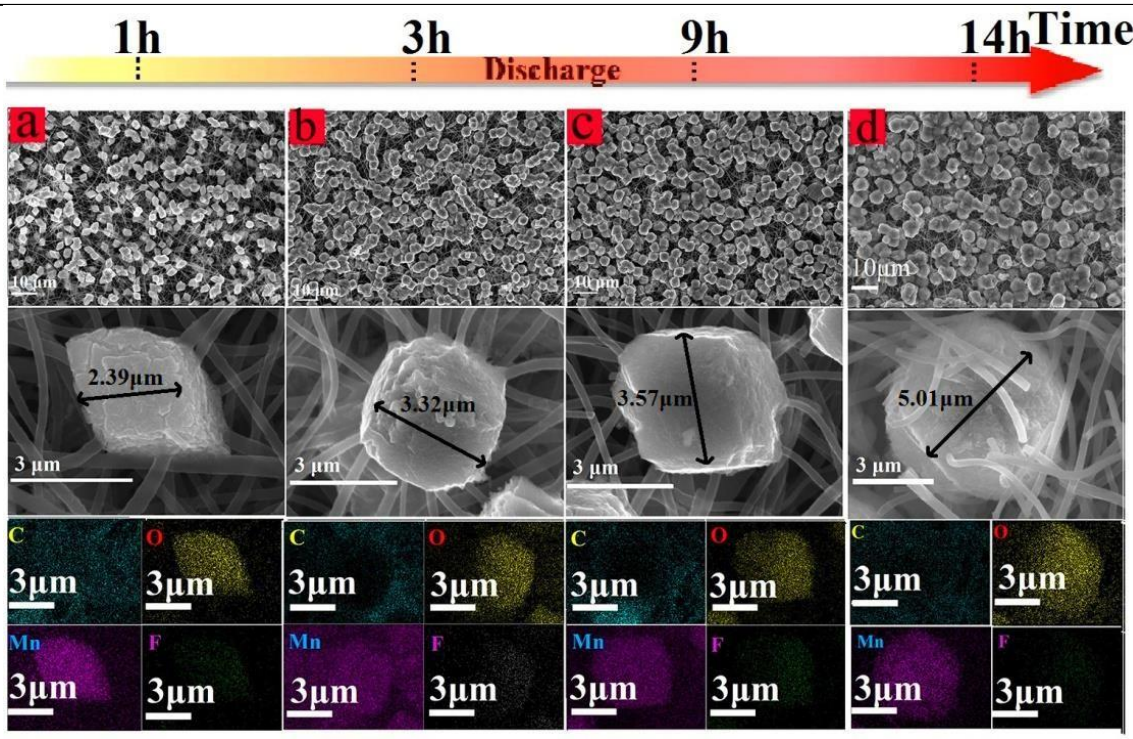

Figure 5 Low magnified (the 1st line) and high magnified (the 2nd line) SEM images,and elemental mapping (the 3rd line) of the flexible electrode CNF/MnO at the state of discharging 1 h (a), 3 h (b), 9 h (c), and 12 h (d), respectively. All the cells are operated at 50 mA g^{-1}.

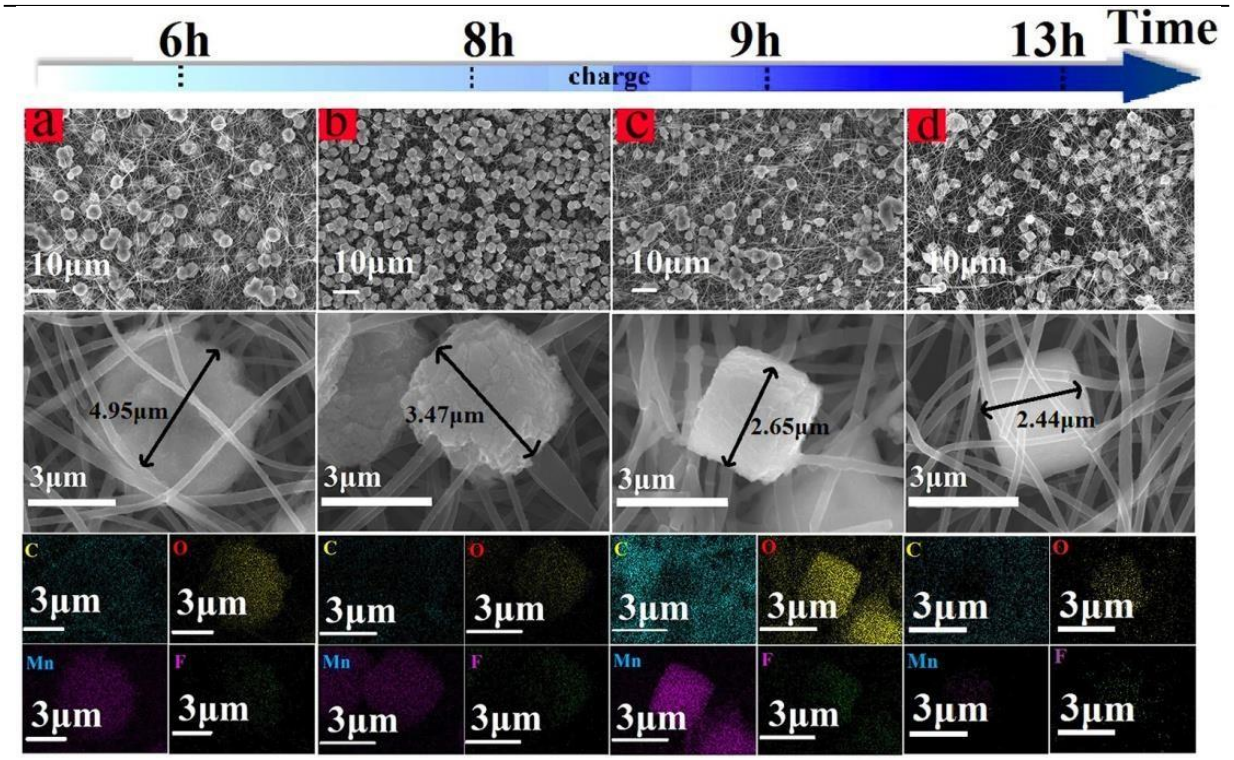

Figure 6 Low magnified (the 1st line) and high magnified (the 2nd line) SEM images, and elemental mapping (the 3rd line) of the flexible electrode CNF/MnO at the state of charging 6 h (a), 8 h (b), 9 h (c), and 11 h (d), respectively. All the cells are operated at 50 mA g^{-1}.

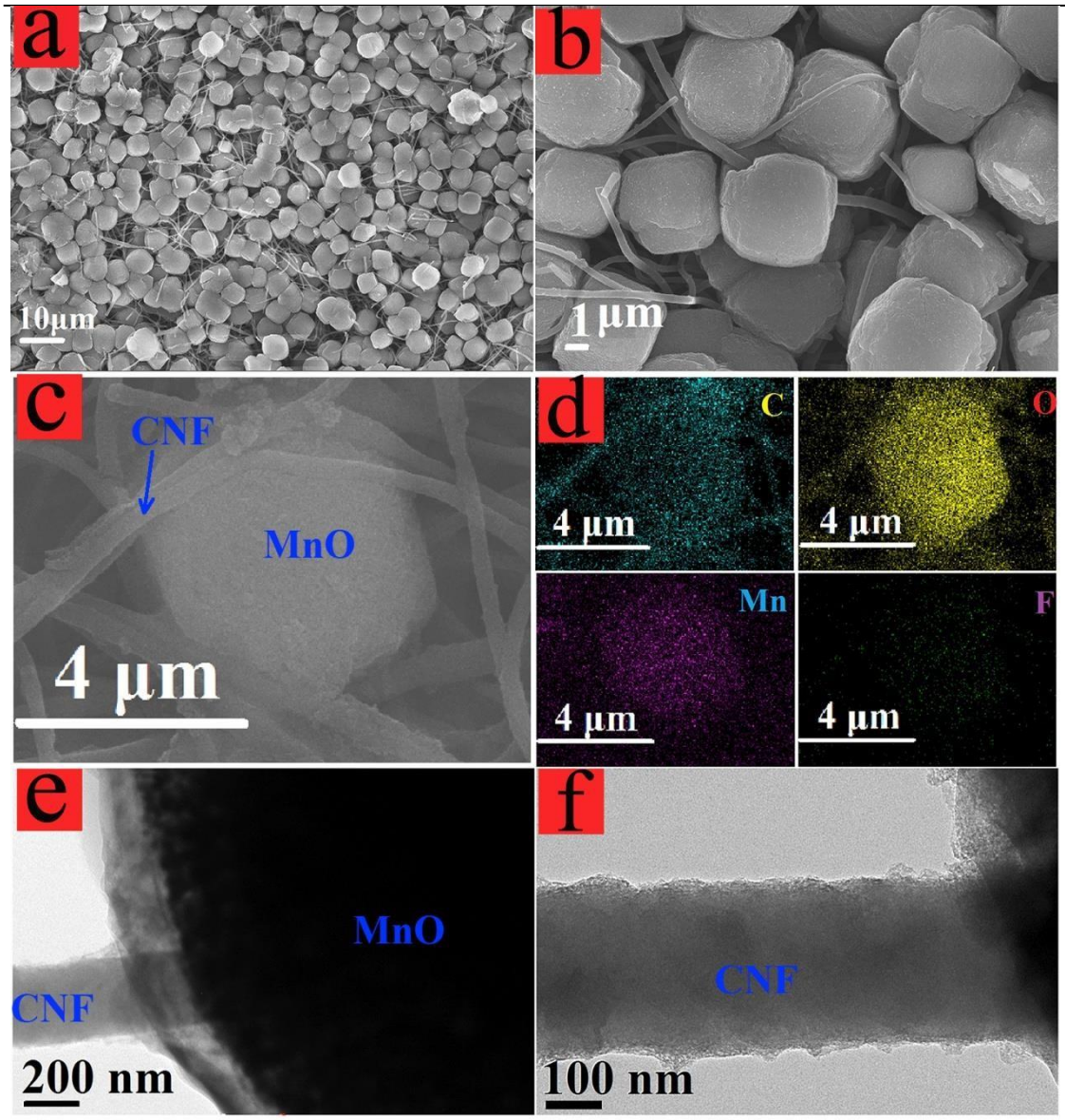

Figure 7 Low magnified (a) and high magnified (b) SEM images, elemental mapping (c, d), and TEM images (e, f) of the flexible electrode CNF/MnO at the state of 50th discharge.

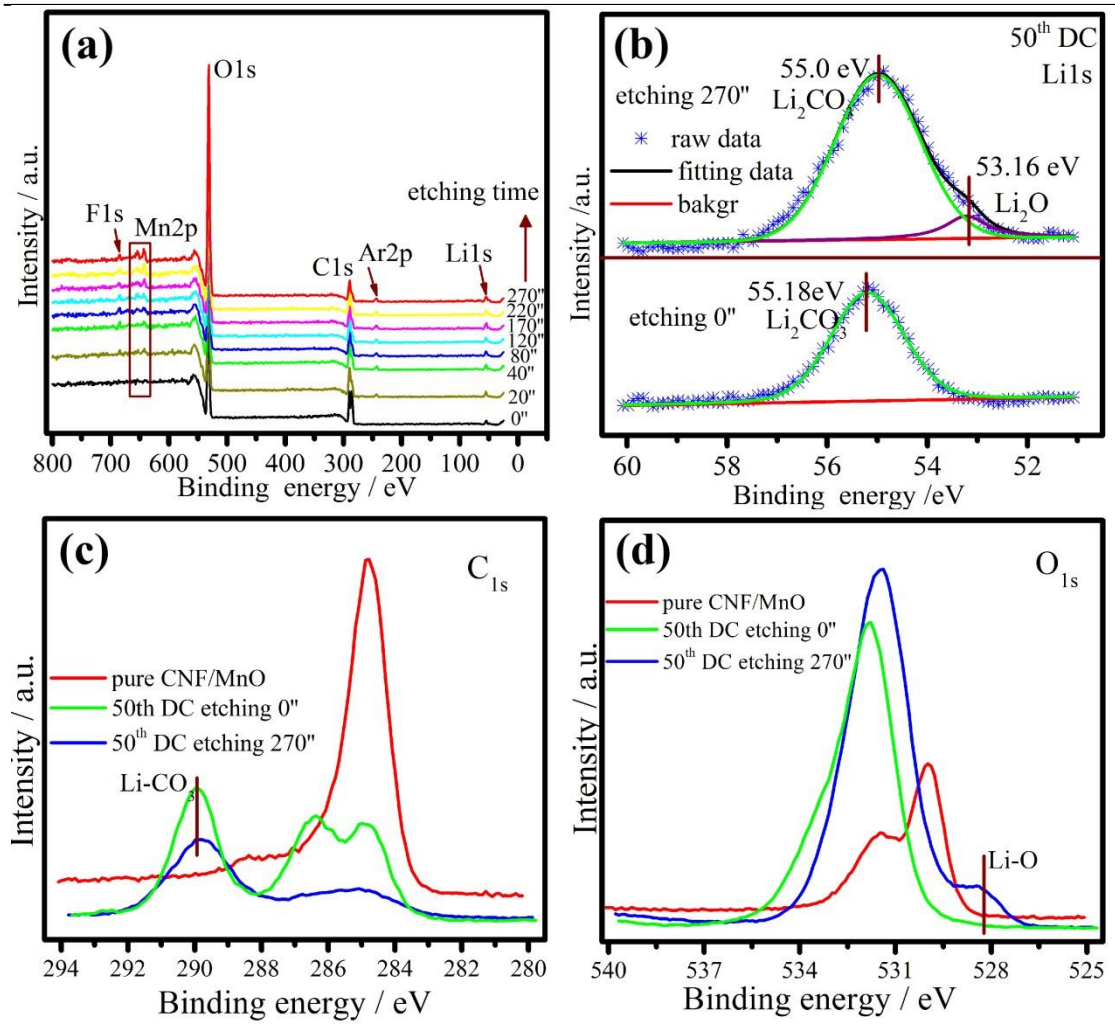

Figure 8 XPS wide scan survey of an electrode CNF/MnO at the state of 50th discharging after Ar^+ etching for 0 - 270 s (a). XPS spectrum Li 1s (b), C 1s (c), and O 1s (d) without Ar^+ etching and with 270 s Ar^+ etching.